

Measuring Near-Field Radiative Heat Transfer in a Graphene-SiC Heterostructure


Naeem Iqbal,^{1,‡} Sen Zhang,^{1,‡} Shuai Wang,^{2,‡} Zezheng Fang,³ Yaoyuan Hu^{①,2}, Yongdi Dang,¹ Minjie Zhang,³ Yi Jin,¹ Jianbin Xu^{①,4}, Bin Feng Ju,^{2,*} and Yungui Ma^{①,†}

¹State Key Lab of Modern Optical Instrumentation, Centre for Optical and Electromagnetic Research, College of Optical Science and Engineering, International Research Center for Advanced Photonics, Zhejiang University, Hangzhou, China

²The State Key Lab of Fluid Power Transmission and Control, School of Mechanical Engineering, Zhejiang University, Hangzhou, China

³Zhejiang Province Key Laboratory of Quantum Technology and Device, Department of Physics, Zhejiang University, Hangzhou, China

⁴Department of Electrical and Electronic Engineering, The University of Hong Kong, Pokfulam Road, Hong Kong, China

 (Received 1 June 2022; revised 5 January 2023; accepted 9 January 2023; published 7 February 2023)

Near-field radiative heat transfer between closely placed objects may exceed the far-field black-body radiation limit by orders of magnitude, especially between polaritonic materials. Great efforts have been made to experimentally measure this fundamental effect in various systems. In this work, we manage to experimentally characterize the near-field thermal emission between less explored plasmon-phonon hybrid material systems made of a graphene-SiC heterostructure. The experiment is carried out using a custom-designed all-optical measurement setup. A heat flux enhancement factor of 26 over the black-body radiation limit is obtained at a 150-nm vacuum gap. Three fundamental modes, i.e., surface plasmon and phonon polaritons with frustrated modes, are identified to contribute the near-field heat flux in this hybrid system. The measured results are well reproduced from the analytical calculations, indicating the robustness of the measurement. Deeper experimental explorations for near-field heat transfer between more complicated material systems could be encouraged in the future.

DOI: [10.1103/PhysRevApplied.19.024019](https://doi.org/10.1103/PhysRevApplied.19.024019)

I. INTRODUCTION

Near-field radiative heat transfer (NFRHT) between closely spaced objects may exceed the far-field Planck's black-body radiation limit by orders of magnitude due to the contribution of evanescent waves [1,2], in particular when there exist bounded surface modes such as surface plasmon polaritons (SPPs) [3,4], surface phonon polaritons (SPhPs) [5,6], or localized waves from hyperbolic materials [7–9]. They may lead to important applications such as thermal rectification [10–12], image sensing [13,14], radiative cooling [15–17], or thermophotovoltaics [18–21]. In recent years, numerous ideas with the combination of two-dimensional (2D) materials or artificial nanostructures have been considered to deepen the physical understanding of near-field thermal radiation [22–26]. Among them, monolayer graphene has received special

attention in tailoring thermal photons due to outstanding features such as infrared SPPs, tunable conductivity, high integration freedom with other species, etc. [27,28]. For example, it could be coupled with a polar material to form a plasmon-phonon hybridized polariton to acquire versatile electromagnetic features [29–31] or with a semiconductor to form a heterojunction to collect thermal photons [32,33]. Recently, graphene/SU8 multilayer heterostructures were also explored to achieve dynamic control over the tunneling of near-field thermal photons [34].

On the other hand, it is still a rather challenging task to precisely characterize the near-field thermal radiation, although measurement capabilities have progressed significantly in the last decade [35–39]. For graphene, the gap distance needs to be controlled in order to improve the coupling of highly localized SPPs. In previous experiments [40–45], electric contacts have often been used to control temperatures and sense heat flux. This is not desired for measuring small samples such as a piece of high-quality 2D material, where electric contacts would significantly complicate the calibration process. For 2D

*mbfju@zju.edu.cn

†yungui@zju.edu.cn

‡These authors contributed equally to this work.

materials or metamaterials, which are usually available only in millimeter or even smaller sizes, an electrodeless measurement is highly desired. All-optical measurement for the NFRHT has previously been successfully applied to detecting the heat transfer from a submillimeter-sized Si emitter [19].

In this work, we employ an all-optical wireless approach to characterize the near-field thermal radiation between plasmon-phonon hybrid photonic nanostructures made of a graphene (gra) covered polar semiconductor 6H-SiC, i.e., forming a gra-SiC heterostructure via van der Waals forces. The emitting sample has a surface area of $1 \times 1 \text{ mm}^2$ and is separated from the identical receiver by a vacuum gap distance of 150 nm realized by nanopillar spacers. The measurement technique developed here has advantages in characterizing 2D materials or metamaterials with limited lateral sizes. A large heat flux exceeding the black-body radiation limit by a factor of 26 at a temperature difference of 45 K is experimentally achieved. The measured temperature-dependent behavior shows good agreement with the theoretical prediction. The contributions from three channels related to the couplings of SPPs, SPhPs, and frustrated modes are identified to be responsible for the enhanced NFRHT.

II. EXPERIMENTAL PROCEDURE AND CHARACTERIZATION

As mentioned previously, the NFRHT between 2D materials has been extensively investigated in theory. Our current intention is mainly on the experimental part,

which has been less studied especially for hybrid polaritonic structures. We explore the heterostructure made of graphene and polar semiconductor silicon carbide, which has SPP and SPhP responses in the infrared spectrum. A Schottky junction is expected to appear at the interface due to the relative work functions [46,47], which could offer an unprecedented measure to control and recycle the near-field heat flux. In this work, an intrinsic SiC single crystal is utilized to better understand the plasmon-phonon interactions and their roles in mediating the near-field thermal radiation.

Figure 1(a) gives a schematic for the all-optical wireless near-field heat flux measurement setup developed here for small samples. The emitter (top) has a total area of $1 \times 1 \text{ mm}^2$, which is far smaller than the receiver (bottom) ($16 \times 16 \text{ mm}^2$). These two ends are separated at a fixed gap distance of 150 nm with the help of photoresist (SU8, thermal conductivity of $0.3 \text{ Wm}^{-1}\text{K}^{-1}$) nanopillars. Similar to previous works, magnets are added to both the emitter and receiver sides to apply a proper contact force [9,32]. A commercial graphene monolayer grown by chemical vapor phase deposition (CVD) (7440-44-0, XFNANO Mater Tech Co., Ltd, China) is utilized here by following the standard transfer procedure. In our device, the emitter is heated by an external laser focused onto one side of a magnet ($1 \times 1 \times 1 \text{ mm}^3$) coated with the black-body paste (with emissivity approximately equal to 1) and the receiver is maintained at room temperature utilizing a thermoelectric cooler (1-12705, Realplay, China). The temperatures of emitter and receiver are in-time monitored by a top thermograph (HPM 11, HIKIMICRO, China) [Fig. 1(b)] via a top infrared window at an uncertainty

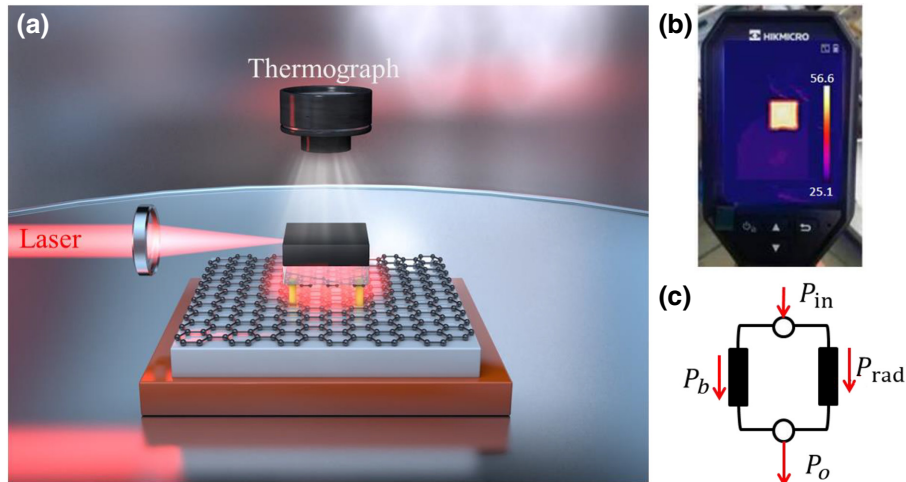


FIG. 1. Measurement setup. (a) Schematic of the all-optical NFRHT measurement setup, where a laser heating source is focused on the emitter and the temperatures are captured by a thermograph. (b) Image from temperature measuring thermograph. (c) Equivalent measurement thermal circuit. The input laser power P_{in} is divided into the near-field radiation P_{rad} and the background dissipation power P_b . The latter includes the far-field radiation power P_{FF} and the heat conduction along the spacing photoresist pillars P_{AZ} . P_o is the dissipation power into the heat sink.

of 0.1 K. An infrared microdomain lens is applied here to acquire a high spatial resolution of about $50\ \mu\text{m}$. The whole experiment is performed in a 1000-class clean room while the NFRHT measurement is conducted at a vacuum pressure of around 10^{-5} Pa. Here, a 532-nm high-stability laser is used with a maximum power of 200 mW, and its stability is 0.1% after 8 h of use. In the experiment, the laser power varies from 2.5 to 15 mW, *in situ* measured by a power meter (PM100D, Thorlabs, USA, with measurement uncertainty of $\pm 3\%$). The input power calibration is carried out before measurement.

As indicated by the equivalent thermal circuit [Fig. 1(c)], the loaded laser input power P_{in} is dissipated through two paths: background loss P_b and thermal radiation P_{rad} , i.e., $P_{\text{in}} = P_{\text{rad}} + P_b$. The background loss includes the heat conduction along the supporting nanopillars P_{AZ} and the far-field radiation into the surrounding environment P_{FF} , i.e., $P_b = P_{\text{AZ}} + P_{\text{FF}}$. The far-field radiation is independent of gap distance [43] and evaluated using the

Stefan-Boltzmann law. By our setup, the near-field heat flux is obtained via $P_{\text{rad}} = P_{\text{in}} - P_{\text{FF}} - P_{\text{AZ}}$. In our experiment, P_{AZ} is directly calculated and P_{FF} is determined from measuring the thermal loss of a standard sample made of a bare SiC (receiver) and Ag/SiC (emitter) pair also with a 150-nm gap, which is assumed to have negligible near-field thermal radiation. The far-field radiation is determined as $P_{\text{FF}} = \sigma \varepsilon_{\text{BB}} \varepsilon_{\text{VC}} (T_e^4 - T_r^4) A_{\text{FF}}$, where σ , A_{FF} , and ε_i ($i = \text{BB}, \text{VC}$, representing black body and vacuum chamber) are the Stefan-Boltzmann constant, radiation area, and emissivity, respectively. Also, the quantities T_e and T_r are the temperatures of the emitter and the receiver, respectively. A layer of silver is deposited on the surface of the emitter to minimize the influence of P_{rad} and thus the SiC-Ag/SiC pair could calibrate the quantity of other branches in a similar temperature range. Here, the effective emissivity of the vacuum chamber is experimentally calibrated through the SiC-Ag/SiC pair as 0.21. The far-field radiation area A_{FF} consists of a total of nine surfaces

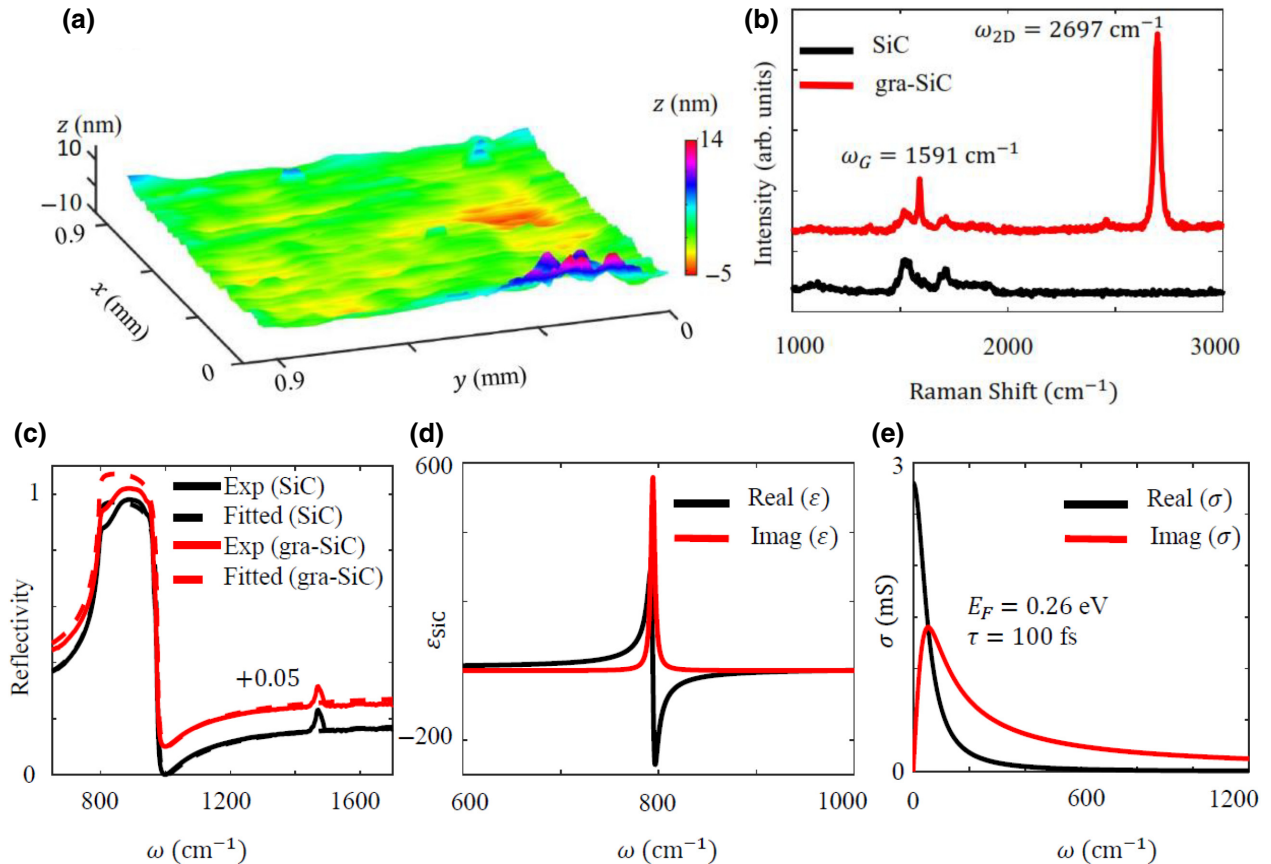


FIG. 2. Material property characterization. (a) Roughness and surface curvature characterization of $1 \times 1\ \text{mm}^2$ gra-SiC heterostructure. (b) Raman spectra of SiC without (black) and with (red) graphene. For graphene, two peaks at $\omega_G = 1591\ \text{cm}^{-1}$ and $\omega_G = 2697\ \text{cm}^{-1}$ are indicated. (c) Measured reflectivity for SiC without (solid black) and with (solid red) graphene. Respective dashed lines are obtained using Lorentz dielectric constant model for SiC and Drude dielectric constant model for graphene. Multiplication by a factor of 0.05 for the heterostructure is used for better visualization. (d) Real and imaginary parts of dielectric constant derived for SiC (fitting parameters: $\varepsilon_\infty = 6.7$, $\omega_{\text{LO}} = 1.8355 \times 10^{14}$ rad/s, $\omega_{\text{TO}} = 1.4989 \times 10^{14}$ rad/s, $\gamma = 8.972 \times 10^{11}$ rad/s). (e) Real and imaginary parts of conductivity derived for graphene (fitting parameters: $E_F = 0.26$ eV and $\tau = 100$ fs).

at the emitter side (four side surfaces of the emitter, each of area $0.5 \times 1 \text{ mm}^2$, and five surfaces of the magnet, each of area $1 \times 1 \text{ mm}^2$) and its value is calculated to be 7 mm^2 . The conduction power is $P_{AZ} = k_{AZ} n A_{AZ} \Delta T / d$, where symbols $k_{AZ} = 0.3 \text{ W m}^{-1} \text{ K}^{-1}$, $n = 4$, A_{AZ} , d , and ΔT represent the thermal conductivity, number of photoresist pillars, cross-sectional area of pillars each having diameter of $3 \mu\text{m}$, height of pillars, and temperature difference, respectively. Among them, the near-field radiation channel takes the major part in heat dissipation. For example, at a temperature difference of 45 K for the gra-SiC pair, the measured value of input power P_{in} is 11.8 mW , radiative power $P_{rad} = 8.8 \text{ mW}$ (75%), $P_{AZ} = 2.5 \text{ mW}$ (21%), and $P_{FF} = 0.5 \text{ mW}$ (4%). Hence, the conduction power is more than 3 times smaller than the near-field radiation power and the far-field power is even smaller. All-optical measurement uncertainty of near-field radiative heat flux could be evaluated with the combined uncertainty u based on the thermal circuit. As the values of P_{AZ} are calculated results, the combined uncertainty u basically relates to the type B uncertainty for P_{in} measurement and u is around 4% for the gra-SiC pair at a temperature difference of 45 K , which is comparable with the electric-based measurement method [32].

In our measurement, the maximum temperature variation is controlled to be smaller than 50 K . Within this range, the variations of infrared properties of both 6H-SiC substrate and graphene could be neglected. The substrate bend including the surface roughness of the gra-SiC sample is smaller than 11 nm as measured by a three-dimensional (3D) optical profiler (NewView 8000 Series, ZYGO, USA) over the area of 1 mm^2 [Fig. 2(a)]. The Raman spectrum of the sample is given in Fig. 2(b). Several peaks between 1400 and 1800 cm^{-1} are observed arising from the longitudinal and transverse optical phonons of 6H-SiC (0001) (lattice texture is decided by the x-ray diffraction measurement). For graphene, a typical G-band peak from the in-plane lattice vibration is observed at 1591 cm^{-1} and the double-resonant 2D-band peak at 2697 cm^{-1} , consistent with earlier reports for epitaxially grown monolayer graphene on a SiC substrate [48]. The monolayer nature of graphene can be derived from the strong 2D-band peak [49]. In addition, the absence of a D-band peak implies our graphene monolayer has very weak residual defects.

The reflection spectra of the samples measured by Fourier transform infrared spectroscopy (FTIR) are plotted in Fig. 2(c). For better visualization, the reflectivity of the gra-SiC sample is shifted upward by 0.05 . As indicated by the dashed lines, the Lorentz model for SiC ($\epsilon_{SiC} = \epsilon_{\infty} [(\omega^2 - \omega_{LO}^2 + i\omega\gamma) / (\omega^2 - \omega_{TO}^2 + i\omega\gamma)]$) and Drude model for graphene ($\sigma_{gra} = (ie^2 |E_F|) / (\pi \hbar^2 (\omega + i\tau^{-1}))$) are utilized to fit the measured reflection data. From this operation, we obtain the parameters $\epsilon_{\infty} = 6.7$, $\omega_{LO} = 1.8355 \times 10^{14} \text{ rad/s}$, $\omega_{TO} = 1.4989 \times 10^{14} \text{ rad/s}$,

$\gamma = 8.972 \times 10^{11} \text{ rad/s}$ for SiC and $\hbar = 1.0546 \times 10^{-34} \text{ Js}$. As plotted in Fig. 2(d), the permittivity spectra exhibit a prominent TO phonon resonance around 797 cm^{-1} . The Fermi level (E_F) estimated from the G-mode frequency is about 0.26 eV , which is typical for CVD-grown graphene [50], and $\tau = 100 \text{ fs}$. The fitted Fermi level is in good agreement with that derived from the Raman spectral peak. Figure 2(e) plots the real and imaginary conductivities of graphene as a function of frequency. A peak around 52.2 cm^{-1} is found for $\text{Re}(\sigma_{gra})$, which is much lower than the frequency of the TO phonon resonance of SiC. Note the high dielectric constant of SiC has red shifted the plasmonic band of graphene compared with vacuum background. Inversely, as seen in the following, the plasmonic response of the graphene monolayer also affects the phononic dispersion of SiC, thus realizing a hybridization nature. As a key parameter of the near-field radiation, the LDOS of the heterostructure is mutually decided by the plasmonic and phononic responses of the constituent materials.

III. RESULTS AND DISCUSSION

The near-field radiative flux of SiC substrates with and without graphene cover is measured by exploiting our laser-based all-optical setup for several temperature differences ΔT . The measured results (blue and purple dots) are shown in Fig. 3 and the temperature of the receiver

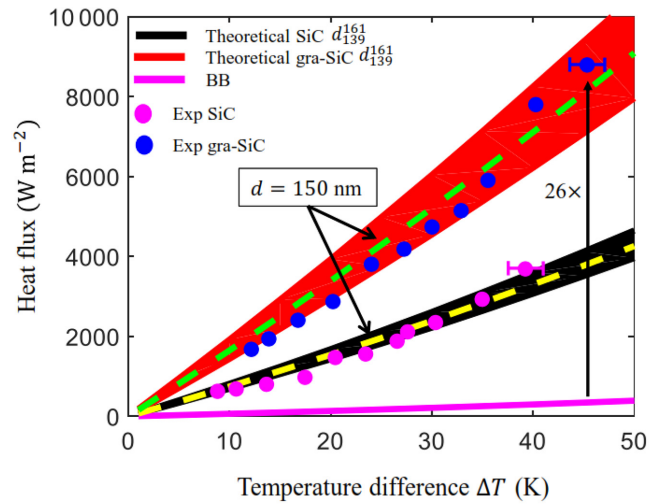


FIG. 3. Measured and simulated results. (a) Theoretical and experimental NFRHT results between identical emitter and receiver made of SiC with (blue) and without (purple) graphene as a function of temperature difference. The experimental results are indicated by circles with bars denoting the measurement uncertainty. The red and black shaded regions are numerically calculated using classic fluctuational electrodynamics incorporating the measurement uncertainties in material and structural parameters. The black-body (BB) radiation (purple) is also given for comparison.

is fixed at 300 K. A gap distance of 150 nm between the emitter and receiver is attained through nanopillars, as depicted in Fig. 5, and the gap distance uncertainty is ± 11 nm. Each experiment takes only few seconds to reach a thermal steady state. The measurement accuracy is around 4%, which is comparable with our previous work [32]. The theoretical results (colored regions in Fig. 3) are calculated based on the fluctuational electrodynamics taking into account the gap distance uncertainty. A good agreement is achieved between the measured and computed results for SiC samples with and without graphene, both showing prominent super-Planckian thermal radiation effects. For example, as indicated by the arrow, at a temperature difference of 45 K, the radiative flux between SiC covered with graphene is enhanced by a factor of around

26 compared with the heat flux between the black bodies. For the case without graphene, this enhancement factor is about 12 for a temperature difference of 40 K.

The preliminary physics behind the near-field enhancement can be understood from the investigation of the LDOS and energy flux spectra. In this context, the LDOS is determined at a distance of 150 nm in free space from the interface of SiC with and without graphene, as shown in Fig. 4(a). Here onward temperature difference and vacuum gap separation are fixed at 45 K and 150 nm, respectively. The resonance peak from the surface phonon polaritons appears at $\omega_{\text{SPhPs}} \approx 951 \text{ cm}^{-1}$ (at this point, $\epsilon_{\text{SiC}} = -1.04 + 0.12i$), which is mostly related to the p -polarized (TM) contribution [51]. The density of states described by the energy density of the black body and spontaneous

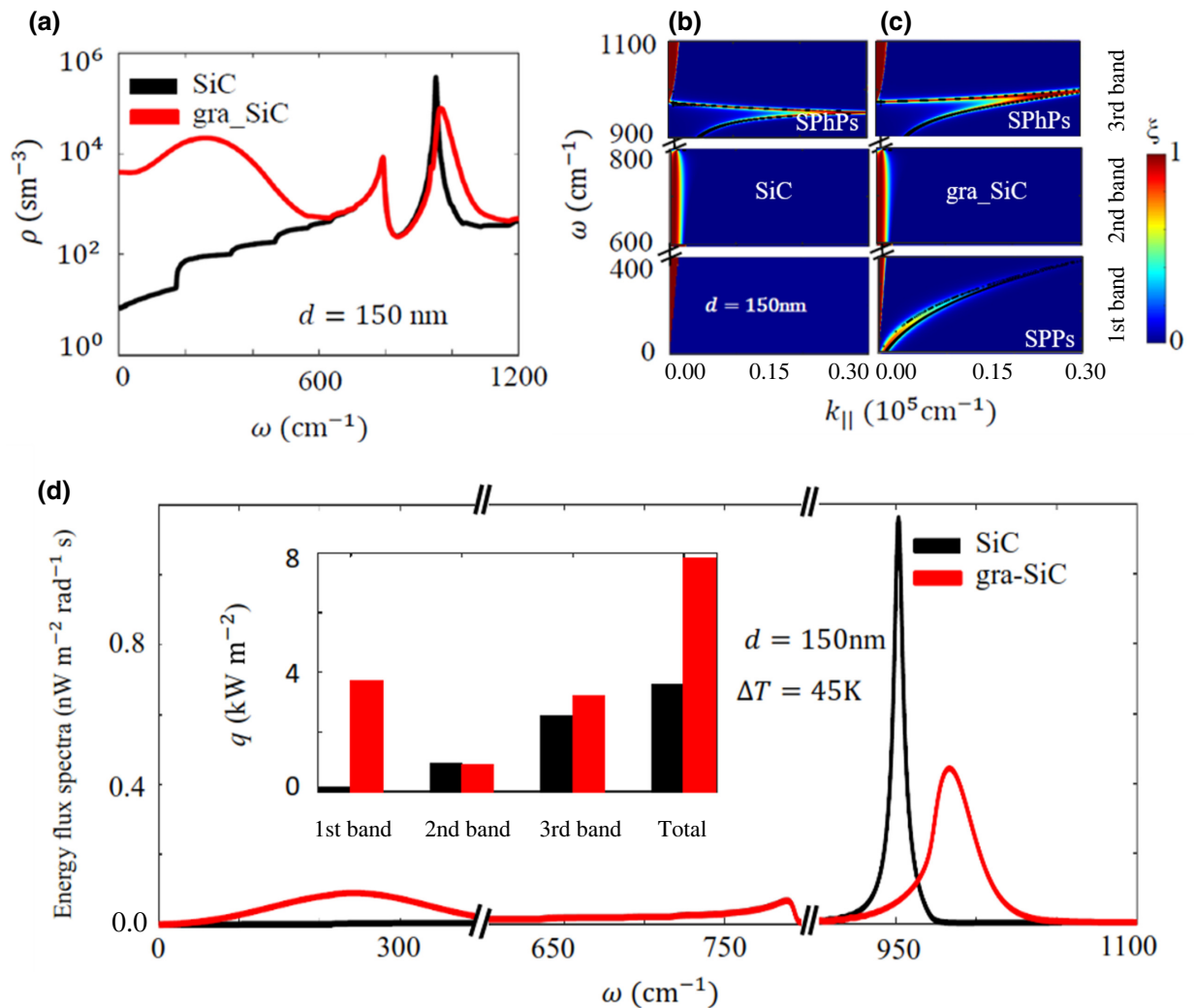


FIG. 4. Spectral mode analysis. (a) LDOS calculated at a distance of 150 nm in free space from the interface of SiC with (red) and without (black) graphene. (b),(c) Energy transmission coefficient ξ for both configurations, i.e., SiC without and with graphene, respectively, as a function of in-plane wave vector $k_{||}$ and angular frequency ω . The black dots represent dispersion relation of graphene SPPs and SiC SPhPs. (d) Energy flux spectra for a separation of 150 nm and temperature difference of 45 K. The inset represents the heat flux integrated for three different subbands.

emission rate can be strongly modulated by surface modes [52,53]. The introduction of graphene could provide strong modulations on the surface optical energy density and thus the near-field heat flux using its high infrared DOS abilities. As shown in Fig. 4(a), the acoustic resonance peak of SiC is broadened and blue shifted to a higher frequency of around 968 cm^{-1} when covered by the monolayer graphene, which has a metallic response in this frequency band. A second DOS peak around $\omega \approx 792 \text{ cm}^{-1} = \omega_T$ is also observed, which is the *s*-polarized (TE) contribution originating from the phonon resonance of SiC [54]. At low frequencies around 255 cm^{-1} , a broad DOS peak is observed owing to the SPP resonance of graphene. Note the plasmonic mode band of graphene is strongly modulated by the high-index SiC substrate. The modulation of the intrinsic model dispersions in the plasmon-phonon hybrid system is evidenced, which also leads to a Fermi level and gap distance dependent NFRHT.

The heterostructure employed here could support three modes: propagating modes ($k_{\parallel} < k_0$), frustrated modes ($k_0 < k_{\parallel} < \varepsilon k_0$), and surface polaritonic modes ($k_{\parallel} > \varepsilon k_0$), with quantities ε , k_{\parallel} , and k_0 denoting material dielectric constant, in-plane wave vector, and free-space wave vector, respectively. Frustrated modes are evanescent in vacuum and propagate inside the material while surface modes are evanescent on both sides. In the current case, the spectrum range could be divided into three portions: $0\text{--}400 \text{ cm}^{-1}$ for SPPs of graphene, $600\text{--}800 \text{ cm}^{-1}$ for frustrated modes of SiC, and $900\text{--}1100 \text{ cm}^{-1}$ for SPhPs of SiC, denoted by first, second, and third bands, respectively. Figures 4(b) and 4(c) plot the transmission coefficient (TC) spectrum between SiC without and with graphene, respectively, as a function of angular frequency and in-plane wave vector. The dispersion curves of the samples are also given by the black dots, calculated from the divergence condition of the transmission coefficients (ignoring material damping) [55], and agree well with the TC spectrum. By comparing the first band of the two samples, graphene's SPP coupling greatly contributes to the energy transmittance in the far-infrared region, indicating the existence of monolayer graphene could efficiently modulate the heat flux. The widespread second band represents the contribution of frustrated modes where the value of the dielectric constant becomes huge. In the third band, a blue shift for the SPhP mode is observed due to the hybridization with the SPP mode of graphene. Owing to material damping, the surface modes are cut off at large k_{\parallel} .

The spectral radiative flux is defined as a function of frequency, which is obtained by Eq. (A2) (Appendix 2) without integration on angular frequency. The result is depicted in Fig. 4(d). A narrow emission peak induced by the SPhPs is observed between bare SiC substrates. The inclusion of graphene makes the difference in radiative flux mediated by SPPs as apparent from the inset figure for heat flux obtained by integrating radiative flux over the

three different frequency bands. The excitation of SPPs in the first band stems from the presence of graphene and their coupling strongly contributes to a large amount of radiative flux as compared with the other bands. For the second band, the spectral heat flux is slightly affected by the introduction of the graphene layer, which perturbs the tunneling of the frustrated modes. For the third band, the phononic emission peak is not only blue shifted but also broadened due to the addition of the conductive graphene monolayer.

IV. CONCLUSION

In summary, near-field heat transfer in a gra-SiC heterostructure is investigated in this work using a homemade all-optical measurement setup. The accuracy of the results is verified by the agreement with the theoretical calculations. We obtain a high radiative heat flux surpassing the far-field black-body radiation limit by 26 times at a gap distance of $150 \pm 11 \text{ nm}$ and temperature difference of 45 K. The LDOS and energy transmission spectral analysis indicate that there exists a strong interaction between the monolayer graphene and the SiC bulk substrate. The introduction of graphene could greatly enhance the heat flux by contributing a highly localized low-frequency plasmonic coupling band. Regarding the robust experimental technique, smaller-sized infrared artificial materials with diverse optical properties could be potentially investigated in the near future, which may pave the way for near-field thermal management, thermophotovoltaic system, and thermal imaging.

ACKNOWLEDGMENTS

The authors thank the partial supports from National Natural Science Foundation of China (Grants No. 62075196, No. 61775195, and No. 61875174), Natural Science Foundation of Zhejiang Province (Grant No. Z21F050013), National Key Research and Development Program of China (Grant No. 2017YFA0205700), and Fundamental Research Funds for the Central University.

N.I. and S.Z. conducted the experiment. S.W. and Y.J. contributed to the sample fabrication. Z.F. and Y.H. contributed to the calculation. M.Z., Y.J., J.X., and B.J. contributed in the data analysis. N.I. prepared the original draft. M.Y.G. contributed in funding accession, project leadership, supervision, writing, reviewing and editing.

The authors declare there is no conflict of interest.

APPENDIX: METHODOLOGY

1. Sample preparation

A single side of a polished 6H-SiC wafer is used and cut into size of $16 \times 16 \text{ mm}^2$. Before transferring the graphene onto the 6H-SiC sample, a standard cleaning process is performed in a sequential manner (5 min ultrasonic bath

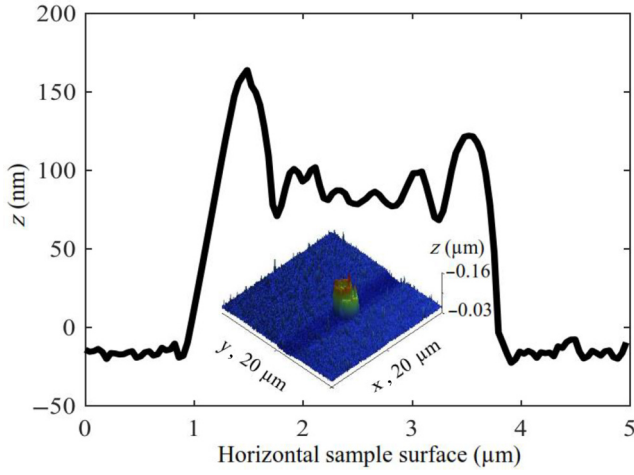


FIG. 5. AFM measurement of nanopillar spacer. Inset shows rebuilt surface topography of the pillar using a 3D profiler.

in acetone and isopropyl alcohols, followed by deionized water and dried using a hydrogen gun). For preparation of the gra-SiC heterostructure, a trivial graphene transfer technique is used [56]. The graphene sheet is first stripped off from the copper substrate and stews above water for about 8 h prior to transfer. Floating graphene is then placed on the SiC sample with the help of tweezers. During the whole process, care must be taken to avoid bubbles on the sheet or any kind of contamination. The graphene carrying sample is left to dry naturally for 30 min and then baked at 95 °C for 12 min. For the emitter, samples of $1 \times 1 \text{ mm}^2$ size are carefully cut with a photoresist protecting cover. On the receiver surfaces of the SiC and gra-SiC heterostructure, SU8-2000.5 photoresist is pinwheel-coated at 4000 rpm for 30 min and then parched for 5 min at 95 °C. The nanopillar arrays are generated by performing the UV photolithography process. Four nanopillar spacers with a period of 500 μm and diameter of 3 μm are fabricated on the receiver surface. Their topologies are characterized by atomic force microscopy (AFM), as shown in Fig. 5. The height lies within the range of 100–150 nm. The value of 150 nm has been used in our calculation, yielding good agreement between simulation and measurement.

2. LDOS and radiative flux calculation

The LDOS including the contribution of the near field and far field is described as [57],

$$\rho(d, \omega) = \frac{\rho_v}{2} \left[\int_0^1 \frac{\kappa d \kappa}{P} \left\{ 2 + \kappa^2 \sum_{l=s,p} \text{Re}(r_l e^{2iP\omega d/c}) \right\} + \int_1^\infty \frac{\kappa^3 d \kappa}{|P|} \left\{ \sum_{l=s,p} \text{Im}(r_l) e^{-2|P|\omega d/c} \right\} \right], \quad (\text{A1})$$

where Re and Im denote the real and imaginary parts, $\rho_v = c(k_0/c\pi)^2$ represents the vacuum density of states, $P = \sqrt{1 - \kappa^2}$ (for $\kappa \leq 1$) and $P = i\sqrt{\kappa^2 - 1}$ (for $\kappa > 1$) is the free-space wave vector, r_l (with $l = s, p$) indicates the Fresnel reflection coefficient for the s - and p -polarizations, and $k_{\parallel} = \omega \kappa / c$ is the wave vector parallel to plane and c is the light speed in the vacuum, where its ranges ($0 \leq \kappa \leq 1$) and ($\kappa > 1$) correspond to the propagating and evanescent waves, respectively.

Regarding the fact that the working wavelength and bending conditions are much smaller than the structure dimensions and the gap distance, the radiative flux between emitter and receiver is evaluated using fluctuational electrodynamics in a semi-infinite planar formation [58],

$$q(\omega, d) = \frac{1}{4\pi^2} \int_0^\infty [\varphi(\omega, T_1) - \varphi(\omega, T_2)] d\omega \int_0^\infty k_{\parallel} \times \sum_{l=s,p} \zeta_l(\omega, k_{\parallel}) dk_{\parallel}, \quad (\text{A2})$$

where the summation in Eq. (A2) gives the contribution of all propagating and evanescent modes depicted by the frequency and parallel to plane wave vector k_{\parallel} of the EM field of both situations, the s - and p -polarizations. Here, the entity $\varphi(\omega, T) = \hbar\omega / [\exp(\hbar\omega/k_B T) - 1]$ illustrates Planck's harmonic oscillator, k_B is Boltzmann constant and the subscript l denotes either s or p , respectively, relying on the s - or p -polarized modes. Moreover, the transmission coefficient ζ_l represents the absolute value of the associated modes participating in heat exchange, and is described as [58],

$$\zeta_l(\omega, k_{\parallel}) = \begin{cases} \frac{(1 - |r_l|^2)^2}{|1 - r_l^2 e^{2ik_{z0}d}|^2}, & k_{\parallel} < k_0 \\ \frac{4[\text{Im}(r_l)]^2 e^{2ik_{z0}d}}{|1 - r_l^2 e^{2ik_{z0}d}|^2}, & |k_{\parallel}| \geq k_0 \end{cases}. \quad (\text{A3})$$

In Eq. (A3), the quantity k_{z0} represents the free-space wave vector. The reflection coefficients r_l associated with the p - and s -polarized waves for the graphene-covered SiC has the following formations:

$$r_p = \frac{k_z^{1p} \varepsilon_2 - k_z^{2p} \varepsilon_1 + (\sigma k_z^{1p} k_z^{2p} / \varepsilon_0 \omega)}{k_z^{1p} \varepsilon_2 + k_z^{2p} \varepsilon_1 + (\sigma k_z^{1p} k_z^{2p} / \varepsilon_0 \omega)}, \quad (\text{A4})$$

$$r_s = \frac{k_z^{1s} - k_z^{2s} - \sigma \mu_0 \omega}{k_z^{1s} + k_z^{2s} + \sigma \mu_0 \omega}. \quad (\text{A5})$$

The variables in Eqs. (A4) and (A5) are described as $k_z^{ns} = k_z^{np} = \sqrt{\varepsilon_n k_0^2 - k_{\parallel}^2}$ with ε_n (with .. denotes the mediums above and below the graphene sheet, respectively), and k_0 is the wave number in free-space. In the case of the

simple SiC substrate without graphene, Eqs. (A4) and (A5) for reflection coefficients are reduced to

$$r_p = \frac{k_z^{1p} \varepsilon_2 - k_z^{2p} \varepsilon_1}{k_z^{1p} \varepsilon_2 + k_z^{2p} \varepsilon_1}, \quad (\text{A6})$$

$$r_s = \frac{k_z^{1s} - k_z^{2s}}{k_z^{1s} + k_z^{2s}}. \quad (\text{A7})$$

In Eqs. (A6) and (A7), ε_1 and ε_2 represent the dielectric constant for free space and the SiC medium, respectively.

3. Dielectric constant

The dielectric constant for SiC is defined as [35,59,60],

$$\varepsilon_2 = \varepsilon_\infty \left[\frac{\omega^2 - \omega_{\text{LO}}^2 + i\omega\gamma}{\omega^2 - \omega_{\text{TO}}^2 + i\omega\gamma} \right]. \quad (\text{A8})$$

The quantities in Eq. (A8) are as follows:

$$\omega_{\text{LO}} = 1.835\ 52 \times 10^{14} \text{ rad/s}, \quad (\text{A9})$$

$$\omega_{\text{TO}} = 1.498\ 97 \times 10^{14} \text{ rad/s}, \quad (\text{A10})$$

$$\gamma = 8.9724 \times 10^{11} \text{ rad/s}, \quad (\text{A11})$$

$$\varepsilon_\infty = 6.7. \quad (\text{A12})$$

Note that SiC is defined as an anisotropic medium; however, the temperature variation in both longitudinal and transverse directions remains similar. Hence, it is treated as isotropic and here only the transverse component is taken into account in the calculations. The dielectric properties for SiC are known and the real and imaginary parts of graphene conductivity can be determined from reflectivity data obtained using FTIR for the gra-SiC heterostructure. The Drude model for graphene conductivity has the following form [61]:

$$\sigma = \frac{ie^2|E_F|}{\pi\hbar^2(\omega + i\tau^{-1})}, \quad (\text{A13})$$

where the value of the Fermi level is obtained as $E_F = 0.26$ eV, which fits well, as shown in Fig. 2(e).

[1] K. Kim, B. Song, V. Fernández-Hurtado, W. Lee, W. Jeong, L. Cui, D. Thompson, J. Feist, M. Reid, and F. García-Vidal, Radiative heat transfer in the extreme near field, *Nature* **14**, 6971 (2015).
 [2] R. St-Gelais, B. Guha, L. Zhu, S. Fan, and M. Lipson, Demonstration of strong near-field radiative heat transfer between integrated nanostructures, *Nano Lett.* **14**, 6971 (2014).
 [3] B. Wang, X. Zhang, X. Yuan, and J. Teng, Optical coupling of surface plasmons between graphene sheets, *Appl. Phys. Lett.* **100**, 131111 (2012).

[4] A. Vakil and N. Engheta, Transformation Optics using Graphene, *Science* **332**, 1291 (2011).
 [5] S. Shen, A. Narayanaswamy, and G. Chen, surface phonon polaritons mediated energy transfer between nanoscale gaps, *Nano Lett.* **9**, 2909 (2009).
 [6] R. Hillenbrand, T. Taubner, and F. Keilmann, Phonon-enhanced light–matter interaction at the nanometre scale, *Nature* **418**, 159 (2002).
 [7] O. D. Miller, S. G. Johnson, and A. W. Rodriguez, Effectiveness of Thin Films in Lieu of Hyperbolic Metamaterials in the Near Field, *Phys. Rev. Lett.* **112**, 157402 (2014).
 [8] S.-A. Biehs, M. Tschikin, and P. Ben-Abdallah, Hyperbolic Metamaterials as an Analog of a Blackbody in the Near Field, *Phys. Rev. Lett.* **109**, 104301 (2012).
 [9] W. Du, J. Yang, S. Zhang, N. Iqbal, Y. Dang, J.-B. Xu, and Y. Ma, Super-Planckian near-field heat transfer between hyperbolic metamaterials, *Nano Energy* **78**, 105264 (2020).
 [10] A. Fiorino, D. Thompson, L. Zhu, R. Mittapally, S.-A. Biehs, O. Bezenecet, N. El-Bondry, S. Bansropun, P. Ben-Abdallah, and E. Meyhofer, A thermal diode based on nanoscale thermal radiation, *ACS Nano* **12**, 5774 (2018).
 [11] E. Moncada-Villa and J. Cuevas, Normal-Metal–Superconductor Near-Field Thermal Diodes and Transistors, *Phys. Rev. Appl.* **15**, 024036 (2021).
 [12] I. Latella, P. Ben-Abdallah, and M. Nikbakht, Radiative thermal rectification in many-body systems, *Phys. Rev. B* **104**, 045410 (2021).
 [13] R. S. DiMatteo, P. Greiff, S. L. Finberg, K. A. Young-Waithe, H. Choy, M. M. Masaki, and C. G. Fonstad, Enhanced photogeneration of carriers in a semiconductor via coupling across a nonisothermal nanoscale vacuum gap, *Appl. Phys. Lett.* **79**, 1894 (2001).
 [14] H. Salihoglu, V. Iyer, T. Taniguchi, K. Watanabe, P. D. Ye, and X. Xu, Energy transport by radiation in hyperbolic material comparable to conduction, *Adv. Funct. Mater.* **30**, 1905830 (2020).
 [15] J. Pérez-Rodríguez, G. Pirruccio, and R. Esquivel-Sirvent, Spectral gaps in the near-field heat flux, *Phys. Rev. Mater.* **3**, 015201 (2019).
 [16] J. Shi, P. Li, B. Liu, and S. Shen, Tuning near field radiation by doped silicon, *Appl. Phys. Lett.* **102**, 183114 (2013).
 [17] X. Xue, M. Qiu, Y. Li, Q. Zhang, S. Li, Z. Yang, C. Feng, W. Zhang, J. G. Dai, and D. Lei, Creating an eco-friendly building coating with smart subambient radiative cooling, *Adv. Mater.* **32**, 1906751 (2020).
 [18] A. Fiorino, L. Zhu, D. Thompson, R. Mittapally, P. Reddy, and E. Meyhofer, Nanogap near-field thermophotovoltaics, *Nat. Nanotechnol.* **13**, 806 (2018).
 [19] T. Inoue, T. Koyama, D. D. Kang, K. Ikeda, T. Asano, and S. Noda, One-chip near-field thermophotovoltaic device integrating a thin-film thermal emitter and photovoltaic cell, *Nano Lett.* **19**, 3948 (2019).
 [20] Y. T. Li, Y. Tian, M. X. Sun, T. Tu, Z. Y. Ju, G. Y. Gou, Y. F. Zhao, Z. Y. Yan, F. Wu, and D. Xie, Graphene-based devices for thermal energy conversion and utilization, *Adv. Funct. Mater.* **30**, 1903888 (2020).
 [21] K. Cui, P. Lemaire, H. Zhao, T. Savas, G. Parsons, and A. J. Hart, Tungsten–carbon nanotube composite photonic crystals as thermally stable spectral-selective absorbers and emitters for thermophotovoltaics, *Adv. Energy Mater.* **8**, 1801471 (2018).

- [22] B. Zhao, C. Guo, C. A. Garcia, P. Narang, and S. Fan, Axion-Field-enabled nonreciprocal thermal radiation in Weyl semimetals, *Nano Lett.* **20**, 1923 (2020).
- [23] A. W. Rodriguez, O. Ilic, P. Bermel, I. Celanovic, J. D. Joannopoulos, M. Soljačić, and S. G. Johnson, Frequency-Selective Near-Field Radiative Heat Transfer between Photonic Crystal Slabs: A Computational Approach for Arbitrary Geometries and Materials, *Phys. Rev. Lett.* **107**, 114302 (2011).
- [24] R. Messina, A. Noto, B. Guizal, and M. Antezza, radiative heat transfer between metallic gratings using Fourier modal method with adaptive spatial resolution, *Phys. Rev. B* **95**, 125404 (2017).
- [25] L. Zhu and S. Fan, Persistent Directional Current at Equilibrium in Nonreciprocal Many-Body Near Field Electromagnetic Heat Transfer, *Phys. Rev. Lett.* **117**, 134303 (2016).
- [26] G. Tang, L. Zhang, Y. Zhang, J. Chen, and C. T. Chan, Near-Field Energy Transfer between Graphene and Magneto-Optic Media, *Phys. Rev. Lett.* **127**, 247401 (2021).
- [27] F. J. Garcia de Abajo, Graphene plasmonics: Challenges and opportunities, *ACS Photonics* **1**, 135 (2014).
- [28] J. C. Cuevas and F. J. García-Vidal, Radiative heat transfer, *ACS Photonics* **5**, 3896 (2018).
- [29] K. Shi, F. Bao, and S. He, Enhanced near-field thermal radiation based on multilayer graphene-hBN heterostructures, *ACS Photonics* **4**, 971 (2017).
- [30] A. Kumar, T. Low, K. H. Fung, P. Avouris, and N. X. Fang, Tunable light-matter interaction and the role of hyperbolicity in graphene-hBN system, *Nano Lett.* **15**, 3172 (2015).
- [31] S. Dai, Q. Ma, M. Liu, T. Andersen, Z. Fei, M. Goldflam, M. Wagner, K. Watanabe, T. Taniguchi, and M. Thiemens, Graphene on hexagonal boron nitride as a tunable hyperbolic metamaterial, *Nat. Nanotechnol.* **10**, 682 (2015).
- [32] J. Yang, W. Du, Y. Su, Y. Fu, S. Gong, S. He, and Y. Ma, Observing of the super-Planckian near-field thermal radiation between graphene sheets, *Nat. Commun.* **9**, 1 (2018).
- [33] I. Shteplyuk, J. Eriksson, V. Khranovskyy, T. Iakimov, A. L. Spetz, and R. Yakimova, Monolayer graphene/SiC Schottky barrier diodes with improved barrier height uniformity as a sensing platform for the detection of heavy metals, *Beilstein J. Nanotechnol.* **7**, 1800 (2016).
- [34] K. Shi, Z. Chen, X. Xu, J. Evans, and S. He, Optimized colossal near-field thermal radiation enabled by manipulating coupled plasmon polariton geometry, *Adv. Mater.* **33**, 2106097 (2021).
- [35] L. Tang, J. DeSutter, and M. Francoeur, Near-field radiative heat transfer between dissimilar materials mediated by coupled surface phonon-and plasmon-polaritons, *ACS Photonics* **7**, 1304 (2020).
- [36] X. Ying, P. Sabbaghi, N. Sluder, and L. Wang, Super-Planckian radiative heat transfer between macroscale surfaces with vacuum gaps down to 190 nm directly created by SU-8 posts and characterized by capacitance method, *ACS Photonics* **7**, 190 (2019).
- [37] P. Sabbaghi, L. Long, X. Ying, L. Lambert, S. Taylor, C. Messner, and L. Wang, Super-Planckian radiative heat transfer between macroscale metallic surfaces due to near-field and thin-film effects, *J. Appl. Phys.* **128**, 025305 (2020).
- [38] B. Song, Y. Ganjeh, S. Sadat, D. Thompson, A. Fiorino, V. Fernández-Hurtado, J. Feist, F. J. Garcia-Vidal, J. C. Cuevas, and P. Reddy, Enhancement of near-field radiative heat transfer using polar dielectric thin films, *Nat. Nanotechnol.* **10**, 253 (2015).
- [39] N. H. Thomas, M. C. Sherrott, J. Brouiliet, H. A. Atwater, and A. J. Minnich, Electronic modulation of near-field radiative transfer in graphene field effect heterostructures, *Nano Lett.* **19**, 3898 (2019).
- [40] J. DeSutter, L. Tang, and M. Francoeur, A near-field radiative heat transfer device, *Nat. Nanotechnol.* **14**, 751 (2019).
- [41] H. Salihoglu, W. Nam, L. Traverso, M. Segovia, P. K. Venuthurumilli, W. Liu, Y. Wei, W. Li, and X. Xu, Near-field thermal radiation between two plates with sub-10 nm vacuum separation, *Nano Lett.* **20**, 6091 (2020).
- [42] K. Shi, Y. Sun, Z. Chen, N. He, F. Bao, J. Evans, and S. He, Colossal enhancement of near-field thermal radiation across hundreds of nanometers between millimeter-scale plates through surface plasmon and phonon polaritons coupling, *Nano Lett.* **19**, 8082 (2019).
- [43] M. Ghashami, H. Geng, T. Kim, N. Iacopino, S. K. Cho, and K. Park, Precision Measurement of Phonon-Polaritonic Near-Field Energy Transfer between Macroscale Planar Structures under Large Thermal Gradients, *Phys. Rev. Lett.* **120**, 175901 (2018).
- [44] J. I. Watjen, B. Zhao, and Z. M. Zhang, Near-field radiative heat transfer between doped-Si parallel plates separated by a spacing down to 200 nm, *Appl. Phys. Lett.* **109**, 203112 (2016).
- [45] K. Ito, A. Miura, H. Iizuka, and H. Toshiyoshi, Parallel-plate submicron gap formed by micromachined low-density pillars for near-field radiative heat transfer, *Appl. Phys. Lett.* **106**, 083504 (2015).
- [46] S. Tongay, M. Lemaitre, X. Miao, B. Gila, B. R. Appleton, and A. F. Hebard, Rectification at graphene-semiconductor interfaces: Zero-gap semiconductor-based diodes, *Phys. Rev. X* **2**, 011002 (2012).
- [47] S. Rajput, M. X. Chen, Y. Liu, Y. Y. Li, M. Weinert, and L. Li, Spatial fluctuations in barrier height at the graphene-silicon carbide Schottky junction, *Nat. Commun.* **4**, 2752 (2013).
- [48] Y. Y. Wang, Z. H. Ni, T. Yu, Z. X. Shen, H. M. Wang, Y. H. Wu, W. Chen, and A. T. Shen Wee, Raman studies of monolayer graphene: The substrate effect, *J. Phys. Chem. C* **112**, 10637 (2008).
- [49] A. C. Ferrari and D. M. Basko, Raman spectroscopy as a versatile tool for studying the properties of graphene, *Nat. Nanotechnol.* **8**, 235 (2013).
- [50] H. Yan, F. Xia, W. Zhu, M. Freitag, C. Dimitrakopoulos, A. A. Bol, G. Tulevski, and P. Avouris, Infrared spectroscopy of wafer-scale graphene, *ACS Nano* **5**, 9854 (2011).
- [51] A. V. Shchegrov, K. Joulain, R. Carminati, and J.-J. Greffet, Near-Field Spectral Effects due to Electromagnetic Surface Excitations, *Phys. Rev. Lett.* **85**, 1548 (2000).

- [52] Y. De Wilde, F. Formanek, R. Carminati, B. Gralak, P.-A. Lemoine, K. Joulain, J.-P. Mulet, Y. Chen, and J.-J. Greffet, Thermal radiation scanning tunnelling microscopy, *Nature* **444**, 740 (2006).
- [53] A. C. Jones and M. B. Raschke, Thermal infrared near-field spectroscopy, *Nano Lett.* **12**, 1475 (2012).
- [54] R. Messina, J.-P. Hugonin, J.-J. Greffet, F. Marquier, Y. De Wilde, A. Belarouci, L. Frechette, Y. Cordier, and P. Ben-Abdallah, Tuning the electromagnetic local density of states in graphene-covered systems via strong coupling with graphene plasmons, *Phys. Rev. B* **87**, 085421 (2013).
- [55] W. B. Zhang, C. Y. Zhao, and B. X. Wang, Enhancing near-field heat transfer between composite structures through strongly coupled surface modes, *Phys. Rev. B* **100**, 075425 (2019).
- [56] A. Abd Latif, N. A. Awang, and Z. Zakaria, Passively mode-locked fiber laser by utilizing TTG film on a D-shaped fiber as a saturable absorber, *J. Sci. Technol.* **9**, 2 (2017).
- [57] K. Joulain, R. Carminati, J.-P. Mulet, and J.-J. Greffet, Definition and measurement of the local density of electromagnetic states close to an interface, *Phys. Rev. B* **68**, 245405 (2003).
- [58] S.-A. Biehs, E. Rousseau, and J.-J. Greffet, Mesoscopic Description of Radiative Heat Transfer at the Nanoscale, *Phys. Rev. Lett.* **105**, 234301 (2010).
- [59] W. Spitzer, D. Kleinman, and D. Walsh, Infrared Properties of Hexagonal Silicon Carbide, *Phys. Rev.* **113**, 127 (1959).
- [60] D. Olego and M. Cardona, Temperature dependence of the optical phonons and transverse effective charge in 3C-SiC, *Phys. Rev. B* **25**, 3889 (1982).
- [61] F. H. Koppens, D. E. Chang, and F. J. García de Abajo, Graphene plasmonics: A platform for strong light-matter interactions, *Nano Lett.* **11**, 3370 (2011).